Effect of polydispersity and bubble clustering on the steady shear viscosity of semidilute bubble suspensions in Newtonian media

Stamatina Mitrou, Simona Migliozzi, Panagiota Angeli, et al.

Citation: Journal of Rheology **67**, 635 (2023); doi: 10.1122/8.0000585
View online: https://doi.org/10.1122/8.0000585
View Table of Contents: https://sor.scitation.org/toc/jor/67/3
Published by the The Society of Rheology

Effect of polydispersity and bubble clustering on the steady shear viscosity of semidilute bubble suspensions in Newtonian media

Stamatina Mitrou, Simona Migliozzi, Panagiota Angeli,[a] and Luca Mazzei[a]

Chemical Engineering Department, University College London Torrington Place, WC1E 7JE London, United Kingdom

(Received 27 September 2022; final revision received 14 February 2023; published 15 March 2023)

Abstract

In this work, we examine the steady shear rheology of semidilute polydisperse bubble suspensions to elucidate the role of polydispersity on the viscosity of these systems. We prove theoretically that the effect of polydispersity on suspension viscosity becomes apparent only if the bubble size distribution is bimodal, with very small and very large bubbles having similar volume fractions. In any other case, we can consider the polydisperse suspension as monodisperse, with the average bubble diameter equal to the De Brouckere mean diameter (d_{43}). To confirm the theoretical results, we carried out steady shear rheological tests. Our measurements revealed an unexpected double power-law decay of the suspension relative viscosity at average capillary numbers between 0.01 and 1. To investigate this behavior further, we visualized the produced bubble suspensions under shear. The visualization experiments revealed that bubbles started forming clusters and threads at an average capillary number around 0.01, where we observed the first decay of viscosity. Clustering and alignment have been associated with shear-thinning behavior in particle suspensions. We believe that the same holds for bubble suspensions, where bubble clusters and threads align with the imposed shear flow, reducing the streamline distortions and, in turn, resulting in a decrease in the suspension viscosity. Consequently, we can attribute the first decay of the relative viscosity to the formation of bubble clusters and threads, proving that the novel shear-thinning behavior we observed is due to a combination of bubble clustering and deformation. https://doi.org/10.1122/8.0000585

I. INTRODUCTION

Suspensions of bubbles in a liquid are often encountered in nature in the form of magmas [1], while they find wide applications in the industry, e.g., in aerated food products [2], cement [3], and personal care products [4]. The gas volume fraction, ϕ, can range from almost zero for very dilute suspensions to more than 0.9 for foams, with most suspensions of practical interest lying in the intermediate range [5].

The presence of bubbles has been shown to change the viscosity of the suspension, inducing shear-thinning and other viscoelastic phenomena, even in Newtonian ambient fluids [5–8]. Consequently, it is important to characterize the rheology of bubble suspensions, providing the industry with useful insight into how aeration affects the viscosity and flowability of various formulations.

For steady shear flows, the effect of bubble volume fraction on the suspension viscosity has been unclear for some time. According to Sibree [9] and Stein and Spera [10], the relative viscosity of a suspension increases with ϕ, while Sura and Panda [11], Bagdassarov and Dingwell [12,13], and Lejeune *et al.* [14] claimed the opposite. Subsequent studies [5,6,8,15] resolved this controversy by identifying two flow regimes, which for simple steady shear flows depend on the *capillary number*,

$$Ca \equiv \frac{\eta_s R \dot{\gamma}}{\sigma_{\alpha,\beta}}, \tag{1}$$

where η_s is the viscosity of the ambient fluid, $\dot{\gamma}$ is the shear rate, R is the radius of a relaxed undeformed bubble, and $\sigma_{\alpha,\beta}$ is the surface tension of the ambient fluid in the gaseous phase [5–8].

The capillary number characterizes the equilibrium configuration of bubbles under steady shear. For $Ca \ll 1$, the suspended bubbles are spherical and obstruct the flow, distorting the fluid streamlines around them; thus, the relative viscosity of the suspension, η_r, increases with ϕ. On the other hand, for $Ca \gg 1$, the bubbles deform significantly and introduce larger slip-free surfaces, which align with the fluid streamlines; as a result, η_r decreases with ϕ. Between the two extremes, the suspension relative viscosity decreases with the shear rate and, in turn, with the capillary number, owing to bubble deformation. For monodisperse bubble suspensions, the onset of the shear-thinning behavior is at values of the capillary number of unit order of magnitude ($Ca \sim 1$). This is shown in Fig. 1. To describe the viscosity of bubble suspensions under steady conditions, researchers have proposed various models where the viscosity is a function of the bubble volume fraction and the capillary number. Llewellin *et al.* [6] suggested a generalized constitutive equation for the rheology of monodisperse bubble suspensions, based on

[a]Authors to whom correspondence should be addressed; electronic mail: p.angeli@ucl.ac.uk and l.mazzei@ucl.ac.uk

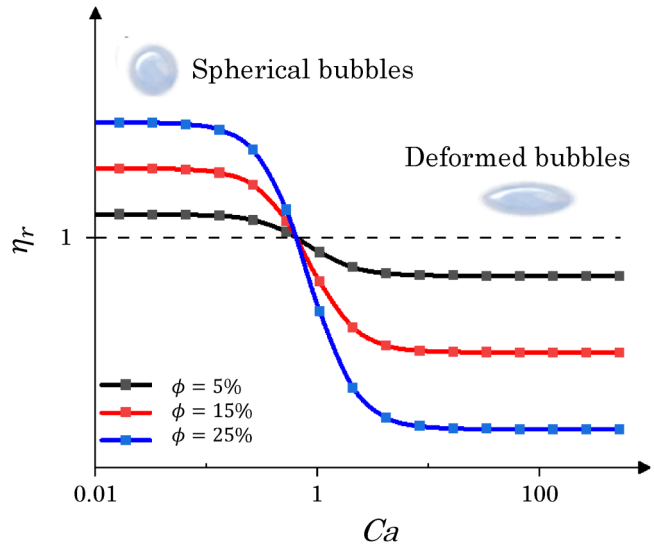

FIG. 1. Relative viscosity as a function of the capillary number Ca and the bubble volume fraction ϕ for a monodisperse bubble suspension.

the analysis of Frankel and Acrivos [16] on the steady shear rheology of dilute monodisperse emulsions. The equation reads

$$\boldsymbol{\sigma} + \lambda_1 \overset{\circ}{\boldsymbol{\sigma}} = 2\eta_s(a\dot{\gamma} + \lambda_2 \overset{\circ}{\dot{\gamma}} + \lambda_3 \ell d[\dot{\gamma} \cdot \dot{\gamma}]), \tag{2}$$

where $\boldsymbol{\sigma}$ is the deviatoric stress tensor; $\dot{\gamma}$ is the rate-of-strain tensor; η_s is the viscosity of the Newtonian ambient fluid; $\overset{\circ}{\boldsymbol{\sigma}}$ and $\overset{\circ}{\dot{\gamma}}$ are the Jaumann derivatives of the stress and rate-of-strain tensors, respectively; the operator ℓd denotes the symmetric traceless part of the tensor on which it operates, while λ_1, λ_2, λ_3, and a are parameters defined as follows, where λ is the relaxation time of a single bubble:

$$\lambda_1 \equiv \frac{6\lambda}{5}, \tag{3a}$$

$$\lambda_2 \equiv \left(1 - \frac{5\phi}{3}\right)\lambda_1, \tag{3b}$$

$$\lambda_3 \equiv \frac{4\phi}{7}\lambda_1, \tag{3c}$$

$$a \equiv 1 + \phi. \tag{3d}$$

Equation (3d) is the Taylor equation [17] for the relative viscosity of dilute bubble suspensions and derives from

$$\eta_r = 1 + \frac{2 + 5\lambda_\eta}{2 + 2\lambda_\eta}\phi, \tag{4}$$

where λ_η is the ratio of the dispersed-phase viscosity to the viscosity of the ambient (Newtonian) fluid. For solid particles, $\lambda_\eta \to \infty$ and Eq. (4) reduces to the Einstein equation [18]. For bubbles, $\lambda_\eta \to 0$ and Eq. (4) becomes equal to $1 + \phi$.

For the case of a simple steady shear flow, Eq. (2) can be solved analytically. In this case, the suspension behaves as a generalized Newtonian fluid with viscosity given by the following constitutive equation:

$$\eta_r = \eta_{r,\infty} + \frac{\eta_{r,0} - \eta_{r,\infty}}{1 + (KCa)^m}, \text{ with K} = 6/5 \text{ and m} = 2, \tag{5}$$

$$\eta_{r,0} = a, \tag{6a}$$

$$\eta_{r,\infty} = \frac{\lambda_2}{\lambda_1}, \tag{6b}$$

where $\eta_r \equiv \eta/\eta_s$, with η equal to the measured viscosity of the suspension, is the relative viscosity of the suspension, $\eta_{r,0}$ is the relative zero-shear viscosity (i.e., the relative viscosity for $Ca \ll 1$), and $\eta_{r,\infty}$ is the relative infinite-shear viscosity (i.e., the relative viscosity for $Ca \gg 1$). Note that by substituting Eq. (3d) in Eq. (6a) the Taylor equation for the zero-shear viscosity of a dilute bubble suspension is obtained [17].

As written above, Eq. (2) is rigorously valid for monodisperse dilute bubble suspensions. Hence, to extend the validity to polydisperse bubble suspensions above the dilute regime, Llewellin *et al.* [5] modified Eq. (3d) to include a fitting parameter

$$a = 1 + b\phi. \tag{7}$$

With this modification, they found good agreement of Eq. (2) to their experimental data for polydisperse systems with bubble volume fractions up to 46%, suggesting an optimal value of $b = 9$. However, their approach was purely empirical and strictly related to their experimental system, thus proving to be inconclusive in terms of evaluating how polydispersity affects the viscosity of bubble suspensions.

According to Mendoza and Santamaría-Holek [19], for dilute suspensions at low capillary numbers, polydispersity does not affect the zero-shear viscosity of the suspension strongly. Mader *et al.* [7] confirmed this statement, claiming that the relative zero-shear viscosity of bubble suspensions obeys the Taylor equation, regardless of polydispersity. Instead, to account for the effect of polydispersity, the authors suggested treating the dilute polydisperse suspension as the sum of N monodisperse components with a characteristic radius R_i and bubble volume fraction ϕ_i. Using Eqs. (5) and (6), one can calculate the relative viscosity for each size class and then sum the individual viscosity contributions $(\eta_{ri} - 1)$ to obtain the relative viscosity of the polydisperse suspension. The authors provided a worked example, but without testing it with experimental data.

Rust and Manga [8] investigated the steady shear viscosity of polydisperse bubble suspensions, considering a surface-weighted average bubble diameter, defined as follows:

$$d_{32} \equiv \frac{M_3}{M_2} \equiv \frac{\int_0^\infty s^3 f(s)\, ds}{\int_0^\infty s^2 f(s)\, ds}, \tag{8}$$

where s is the diameter of the undeformed bubbles and $f(s)$ is the number density function (NDF) of the bubbles. Fitting their rheological data with the Cross model [20], they found good agreement for $K = 0.72$ and $m = 1.43$. For the relative zero-shear viscosity, they used the Krieger–Dougherty equation for solid particles,

$$\eta_{r,0} = \left(1 - \frac{\phi}{\phi_m}\right)^{-B\phi_m}, \tag{9}$$

suggesting the empirical values $\phi_m = 0.6$ and $B = 1$ [this value ensures that Eq. (9) agrees with the Taylor equation, Eq. (3d), in the limit of small values of ϕ], while for the relative infinite-shear viscosity, they proposed the following empirical equation:

$$\eta_{r,\infty} = 1 + c_1\phi + c_2\phi^2, \tag{10}$$

with $c_1 = -1.14$ and $c_2 = -9.8$. Even though the authors accounted for the effect of polydispersity, their approach is not supported by theory and is strongly system dependent.

Morini *et al.* [21] recognized the complexity caused by polydispersity and, thus, designed a microchannel device to produce monodisperse bubble suspensions in Newtonian media. Although there was some variation in the bubble size due to coalescence, the generated suspensions were nearly monodisperse and the bubble volume fraction reached values up to 18%. Investigating the steady shear viscosity of the produced bubble suspensions, they found a good agreement with the predictions of Frankel and Acrivos [16] both in the dilute and the semidilute regimes.

As highlighted above, several studies have focused on the rheology of monodisperse bubble suspensions, advancing constitutive equations for their steady shear viscosity. However, the issue of polydispersity has been sparsely studied, with most of the published papers providing empirical constitutive equations that strongly depend on experimental data. In this work, we aim to clarify the role of polydispersity through theoretical analysis, validated with experimental studies. To this end, we generated semidilute polydisperse bubble suspensions and measured their steady shear viscosity. Our rheological measurements revealed an unexpected double power-law decay of the relative viscosity, a trend that cannot be supported by our theoretical analysis on polydispersity. To investigate this behavior, we visualized the produced bubble suspensions under shear. The rheo-optical experiments revealed the shear induced formation of bubble threads and clusters, which we believe are responsible for the first decay of viscosity. In Sec. II, we present theoretical calculations that clarify the effect of polydispersity on the relative viscosity of semidilute bubble suspensions. We then introduce our experimental methods for the generation, rheological characterization, and visualization of the produced bubble suspensions, followed by the discussion of the results.

II. THEORETICAL ANALYSIS OF THE EFFECTS OF POLYDISPERSITY ON RELATIVE VISCOSITY

To investigate theoretically the effect of polydispersity, we calculated the suspension viscosity for three bubble size distributions. We considered a mixture of mineral oil and 0.57 mol/l span 80 (surfactant), with bubble volume fraction of 10.4% and different bubble sizes. To calculate the relative viscosity of the bubble suspension, we followed the method described in Mader *et al.* [7]. In brief, we calculated the relative viscosity for each ith bubble class using Eqs. (5) and (6), where in Eq. (5), we substituted the capillary number Ca of the suspension with the capillary number Ca_i of the ith size class, and in Eq. (6), we replaced the total volume fraction of bubbles ϕ with that of the ith bubble class, ϕ_i.

To determine ϕ_i, we first calculated the bubble volume for each size class (V_i), then summed the bubble volumes for all the different size classes to attain the total bubble volume in the suspension (V_{tot}) and, finally, calculated the bubble volume fraction for each class (ω_i) and multiplied it by the measured total volume fraction of bubbles in the suspension (ϕ_{tot}),

$$V_i = N_i \frac{4}{3}\pi R_i^3, \quad V_{tot} = \sum_{i=1}^{\nu} V_i, \tag{11}$$

$$\omega_i = \frac{V_i}{V_{tot}}, \tag{12}$$

$$\phi_i = \omega_i \phi_{tot}, \tag{13}$$

where N_i is the number of bubbles in each bubble class and ν is the number of bubble classes. The relative viscosity of the polydisperse suspension is then obtained by linearly combining the individual viscosities of the different bubble classes η_i with the solvent contribution as follows:

$$\eta_i = \eta_{r_i} - 1, \tag{14}$$

$$\eta_r = 1 + \sum_{i=1}^{\nu} \eta_i. \tag{15}$$

For each theoretical example, we plotted the relative viscosity of the suspension as a function of an average capillary number, $\langle Ca \rangle$, defined using the volume-weighted average radius of the undeformed bubble, $\langle R \rangle$, obtained from the De Brouckere average diameter d_{43}, which is the ratio between the fourth and the third moments of the size distribution,

$$d_{43} \equiv \frac{M_4}{M_3} \equiv \frac{\int_0^\infty s^4 f(s)\, ds}{\int_0^\infty s^3 f(s)\, ds}. \tag{16}$$

We consider d_{43} more representative than other average diameters because it accounts for the bubble volume fraction, a property that strongly affects the relative viscosity of the suspension. We would like to clarify that the above approach is valid for dilute systems, where bubble interactions can be

considered negligible. However, after comparing its predictions with our experimental results, we found that it can accurately predict the relative viscosity of semidilute suspensions as well. Thus, the model reported in Mader *et al.* [7] is considered suitable for describing the relative viscosity of the bubble suspensions investigated in this work.

A. Scenario 1—Bimodal distribution ($R_1 = 10\,\mu$m, $R_2 = 500\,\mu$m)

The first scenario concerns a bubble suspension consisting of bubbles with only two radii, 10 and 500 µm. The total bubble volume fraction is equally divided between the small and large bubbles, so that the volume-weighted average radius is equal to 255 µm. Following the procedure explained above, we obtained the viscosity curve shown in Fig. 2.

In this example, the shear-thinning behavior does not occur at $\langle Ca \rangle \sim 1$, as it happens for a monodisperse bubble suspension. Instead, it spans a range of average capillary numbers, between 0.1 and 100. This behavior is due to polydispersity and can be explained by correlating the average capillary number with the capillary number for each size class, as follows:

$$Ca_i \equiv \frac{\eta_s R_i \dot{\gamma}}{\sigma_{\alpha,\beta}} = \frac{\eta_s \langle R \rangle \dot{\gamma}}{\sigma_{\alpha,\beta}} \frac{R_i}{\langle R \rangle} = \langle Ca \rangle \frac{R_i}{\langle R \rangle}, \tag{17}$$

which gives

$$\langle Ca \rangle = \frac{\langle R \rangle}{R_i} Ca_i. \tag{18}$$

For each size class, the bubbles should be deformed significantly when the corresponding capillary number is of order 1, so that the average capillary number is of the order,

$$\langle Ca \rangle \sim \frac{\langle R \rangle}{R_i}. \tag{19}$$

Based on this, the large bubbles with a radius equal to 500 µm should be deformed significantly when $\langle Ca \rangle \approx 0.5$. Therefore, we should expect the first drop in suspension relative viscosity to start at $\langle Ca \rangle \sim 0.1$, as observed in Fig. 2. Likewise, the small bubbles with radius 10 µm should be deformed significantly when $\langle Ca \rangle \approx 25$. Therefore, we should expect the second drop in suspension relative viscosity to start at $\langle Ca \rangle \sim 10$, as observed in Fig. 2. Between the two relative viscosity drops, there is an intermediate plateau, which indicates that the larger bubbles have fully deformed, while the smaller ones are still almost spherical.

Even though this example is extreme, it demonstrates that polydispersity can cause an extended shear-thinning behavior that spans a range of average capillary number values, instead of happening at $\langle Ca \rangle \sim 1$. Moreover, the viscosity curve has a more complex behavior, with a plateau between the two viscosity decays. The presence of the intermediate plateau does not allow us to model this behavior using a constitutive equation for monodisperse suspensions and an average bubble diameter, as the plateau would not appear. In these cases, for dilute and semidilute suspensions, one must operate as we did, considering each bubble class individually, obtaining the viscosity contribution for each class by using the constitutive equation for monodisperse suspensions, and then adding the contributions.

B. Scenario 2—Bimodal distribution ($R_1 = 10\,\mu$m, $R_2 = 200\,\mu$m)

This scenario concerns another bidisperse bubble suspension, with a smaller difference between the two bubble sizes, these being 10 and 200 µm. As in the previous scenario, the two bubble classes contribute equally to the total bubble volume fraction, and the volume-weighted average radius is equal to 105 µm. Following the same method, we obtained the viscosity curve of Fig. 3. As seen, also in this case the shear-thinning part of the curve spans a wider range of $\langle Ca \rangle$ values than that for a monodisperse suspension. However,

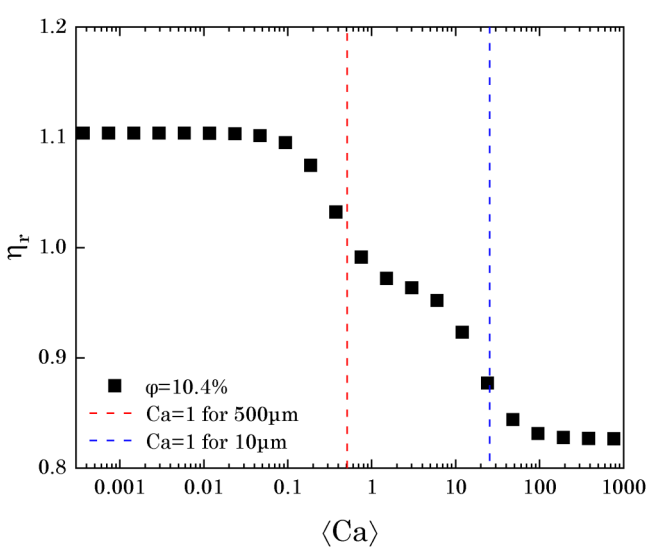

FIG. 2. Relative viscosity versus average capillary number, for $\phi = 10.4\%$ and bubble sizes of 10 and 500 µm with $\omega_1 = \omega_2 = 0.5$.

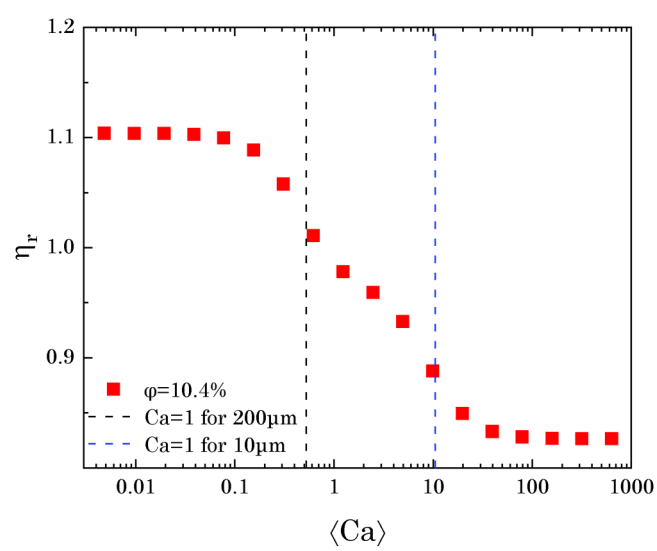

FIG. 3. Relative viscosity versus average capillary number, for $\phi = 10.4\%$ and bubble sizes of 10 and 200 µm with $\omega_1 = \omega_2 = 0.5$.

unlike the first scenario, this range is smaller, between 0.1 and 50. The first decay of the relative viscosity again starts at $\langle Ca \rangle \sim 0.1$ and indicates the deformation of the 200 μm bubbles. The second viscosity drop starts at $\langle Ca \rangle \sim 1$ and is correlated with the deformation of the 10 μm bubbles. The intermediate plateau of viscosity still exists but is less noticeable than in the first example. Thus, the effect of polydispersity becomes more evident when the difference in bubble size increases.

C. Scenario 3—Gamma-type distribution (bubble sizes between 10 and 170 μm)

The last scenario refers to our experimental data, with bubble radii following a gamma distribution between 10 and 170 μm [Fig. 4(a)], and $\langle R \rangle = 82.5$ μm. The limits of the size distribution are similar to those in scenario 2; however, in this case, the total bubble volume fraction is not equally divided between the small and large sizes. Instead, each size class between the smallest (10 μm) and largest (170 μm) size values corresponds to a percentage of the total bubble volume fraction. Calculating the relative viscosity of the polydisperse suspension, we obtained the viscosity curve of Fig. 4(b) (green points). As seen, the shear-thinning behavior happens over a range of capillary number values where, for most values, the order of magnitude of $\langle Ca \rangle$ is unity and, in contrast to the two systems previously analyzed (scenarios A and B), it does not extend further than this region. There is no intermediate plateau, and the viscosity curve closely resembles that of a monodisperse suspension. This rheological trend is similar to what is observed in polymer melts, where a polydisperse molecular weight distribution leads to a relaxation time spectrum that can be represented by a weighted average relaxation time [22]. To validate this, we calculated the viscosity curve of a monodisperse suspension with a bubble radius equal to 82.5 μm, using Eqs. (5) and (6) [Fig. 4(b)—red curve]. As seen, the two viscosity curves almost coincide. Thus, we can conclude that polydispersity can significantly affect the suspension viscosity only if the total bubble volume fraction is divided between very small and very large bubbles—a condition that is rarely met experimentally. Under usual experimental conditions, where the bubble sizes follow the gamma distribution, the effect of polydispersity is not profound, and we can regard the polydisperse suspension as monodisperse with a volume-weighted average bubble diameter.

III. MATERIALS AND METHODS

A. Chemicals

RTM32 Mineral Oil Rotational Viscometer Standard (Paragon Scientific, Birkenhead, UK) is a Newtonian oil, with a viscosity of 9.274 Pa s. Span 80 (Sigma Aldrich, St. Louis, USA) is a liquid, nonionic surfactant (molecular weight: 428.61 g/mol; density at 20 °C: 1 g/cm^3). To generate stable bubble suspensions, we used a mixture of mineral oil and 0.57 mol/l of Span 80. We chose this as ambient fluid because it is Newtonian and it allows the generation of small bubbles and stable suspensions. The properties of the individual chemicals and the final mixture are summarized in Table I.

B. Generation and rheological characterization of bubble suspensions

To produce the bubble suspensions, we designed and manufactured an aeration device offering simultaneous aeration and mixing [Fig. 5(a)]. The system consists of a propeller with attached aeration plates, covered with ceramic filters with a characteristic porosity dimension of 2 μm. The propeller rotates, distributing the bubbles in the ambient fluid and producing homogenous suspensions. The aeration time depended on the desired volume fraction; longer aeration times led to denser suspensions. After generating the bubble suspensions, we mixed them at high-shear rates (Silverson, L5 Series high-shear mixer) to reduce the bubble size.

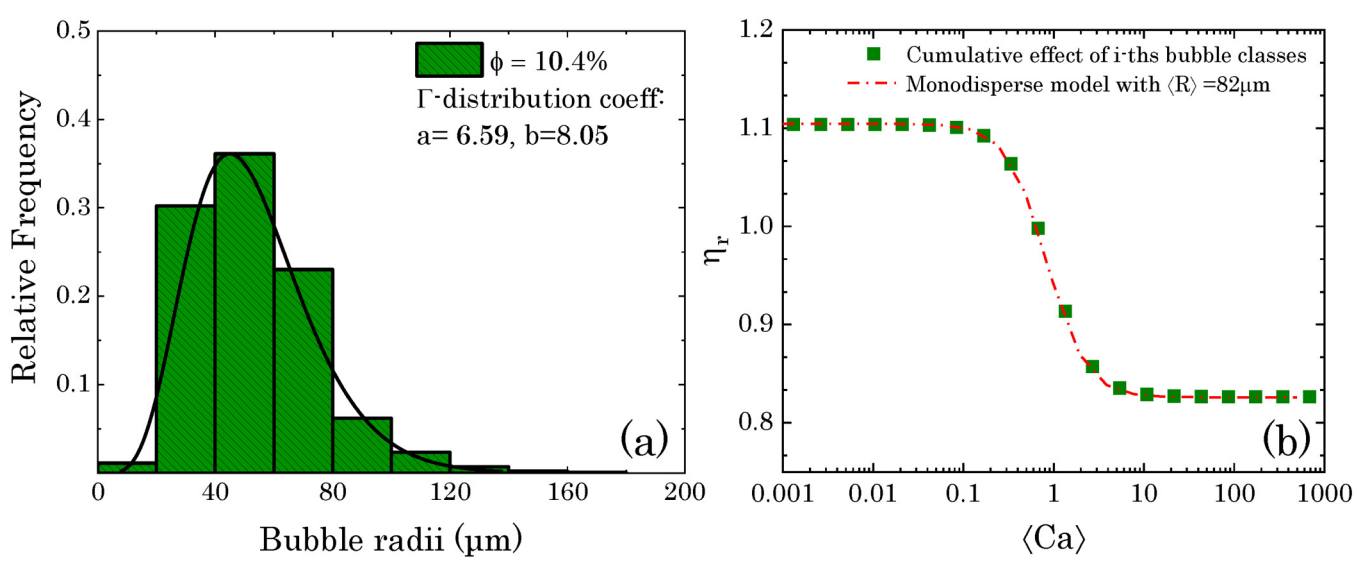

FIG. 4. (a) Gamma-type bubble size distribution (10–170 μm); (b) relative viscosity versus $\langle Ca \rangle$ number for $\phi = 10.4\%$ and bubble sizes following a gamma distribution between 10 and 170 μm.

TABLE I. Viscosity η, density ρ, and surface tension $\sigma_{\alpha,\beta}$ of fluids used to prepare the Newtonian ambient fluid.

	η (Pa s)	ρ (g/ml)	$\sigma_{\alpha,\beta}$ (mN/m)
RTM32 mineral oil	9.274	0.860	32.363
Span 80	1.946	0.986	29.340
Mixture	4.230	0.887	29.986

Afterward, we left the suspensions to rest until their temperature reached that of the ambient fluid before the aeration, then we calculated the bubble volume fraction gravimetrically, weighting 50 ml of bubble suspension and using the following equation:

$$\phi = 1 - \frac{\rho_{suspension}}{\rho_{ambient\ fluid}}. \tag{20}$$

Images of all generated bubble suspensions were recorded with a bright field optical microscope (Zeiss Axio Observer 5) and analyzed using a Matlab in-house code to determine the bubble size distribution. The rheological tests were carried out in an Anton Paar MCR302 stress-controlled rotational rheometer, equipped with a Peltier plate to control the operating temperature (20 °C), and a sandblasted parallel-plate geometry (with a radius of 20 mm) to avoid wall-slip effects. For all measurements, we set the rheometer gap at 1.9 mm to ensure a gap ten times larger than the average bubble diameter, thus avoiding possible wall effects induced by the plates confinement. To obtain the viscosity curves for the bubble suspensions, we performed steady shear measurements in the range 0.05 to 150 s^{-1}. We operated within the limit of 150 s^{-1} to minimize bubble coalescence and bursting and to keep the bubble volume fraction stable. The samples were carefully analyzed by eye after each measurement to ensure that no material was spurted out of the geometry during the rheological experiments. The Weissenberg–Rabinowitsch correction [22] was applied to account for the nonuniform shear across the parallel plates. As previously mentioned in Morini *et al.* [21], the radial variation of the shear rate in the parallel-plate geometry causes a linear change of the capillary number from zero to its maximum value at the rim of the geometry. Consequently, bubbles deform differently depending on their position in the measuring plate. The Weissenberg–Rabinowitsch method overcomes the problem arising from the radial change of the shear rate because it considers a value of the shear rate and of the corresponding shear stress *in a specific location*, namely, at the edge of the plates. Hence, we are confident that the radial distribution of shear rates, and in turn of capillary numbers, is not responsible for the rheological trends reported in Sec. IV B.

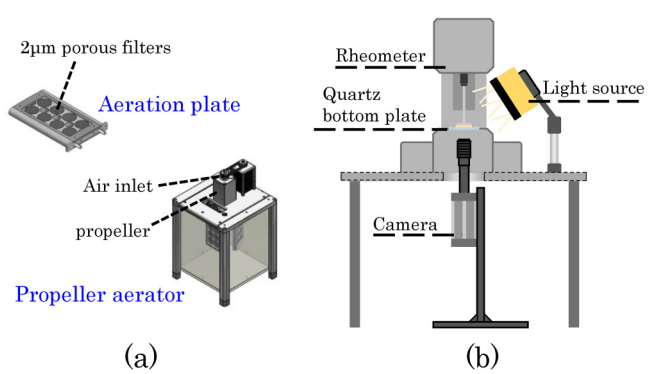

FIG. 5. (a) Schematic of the aeration device used to generate bubble suspensions; (b) rheo-optical setup.

C. Visualization of bubble suspensions under steady shear

To visualize the bubble suspensions under shear, we modified the setup of the rheometer with a glass bottom plate (Anton Paar Peltier Universal Optical Device—P-PTD 200/GL) to allow optical access. During the shear tests, we recorded the images using a Zyla 5.5 sCMOS camera (acquisition frequency: 30 Hz, image resolution: 2560 × 2160 pixels), a Nikon mono zoom lens and a white led light as illumination. To avoid reflections from the metal, we coated the sandblasted parallel plate with black spray paint. A schematic of the visualization setup is given in Fig. 5(b). The recorded images were taken at ≈ 0.6 mm from the bottom plate. To ensure repeatability of the focus plane position, we used transparent laminated sheets of 0.3 mm thickness, which we sticked together to create a disk of 0.6 mm height. We then placed a millimetric scale grid on top of the disk and focused on it. All our rheo-optical experiments were performed at this focus plane, with very small adjustments for different samples. We performed steady shear rheological tests, in the range 0.1 to 50 s^{-1} for a fixed time of 40 s per shear rate, and set the rheometer gap at 1.9 mm, to be consistent with the previous viscosity measurements. However, with this gap, multiple suspension layers formed, preventing a detailed image analysis. Thus, we also conducted experiments with a 0.8 mm gap. Figure 6 shows two representative images, taken with the 1.9 and 0.8 mm gaps. Even if it was difficult to individuate the bubbles accurately in the 1.9 mm images, these still offered insight into the shear-induced phenomena happening in the entire volume of the tested samples, which is relevant to the final viscosity recorded. The 0.8 mm gap images were only used to investigate the bubble size distributions and identify possible coalescence phenomena during shearing, even though we need to stress that bubble coalescence can be enhanced due to the more confined flow.

IV. RHEOLOGICAL MEASUREMENTS

In this section, we present our experimental results for bubble suspensions with volume fractions $\phi_1 = 4.7\%$ and $\phi_2 = 10.4\%$.

A. Bubble size distributions

The tested samples were found to be polydisperse, with bubble radii following the gamma distribution between 10 and 170 μm (Fig. 7). This means that the suspensions consisted mostly of small bubbles, with radii ranging up to 100 μm; even though the larger bubbles were fewer in number, they

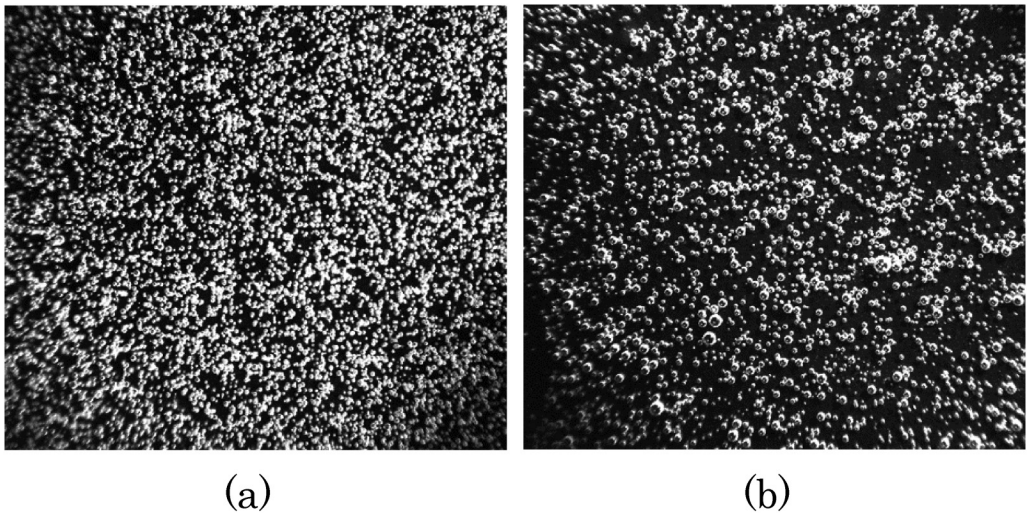

FIG. 6. Bubble suspension ($\phi = 5.6\%$) under steady shear ($1\ \mathrm{s}^{-1}$) with (a) 1.9 mm gap and (b) 0.8 mm gap.

contributed importantly to the total bubble volume fraction. As the suspensions were polydisperse, we used the De Brouckere average diameter d_{43} to characterize them. For the reported bubble volume fractions, $\phi_1 = 4.7\%$ and $\phi_2 = 10.4\%$, d_{43} was equal to 199 and 165 μm, respectively.

B. Steady shear experiments

As shown in Fig. 8, all tested suspensions were characterized by a shear-thinning behavior with a double power-law decay of the suspension relative viscosity. The first decay always happened at shear rates around $1\ \mathrm{s}^{-1}$, corresponding to $\langle Ca \rangle \sim 0.01$, while the second started at shear rates around $20\ \mathrm{s}^{-1}$, corresponding to $\langle Ca \rangle \sim 1$. This double decay was unexpected, because it is not predicted by the rheological models discussed in Sec. II. As discussed, two decays of the relative viscosity—with a plateau between them—appear only if the bubble size distribution is bimodal, with very small and very large bubbles having similar volume fractions. However, this is not the case in our

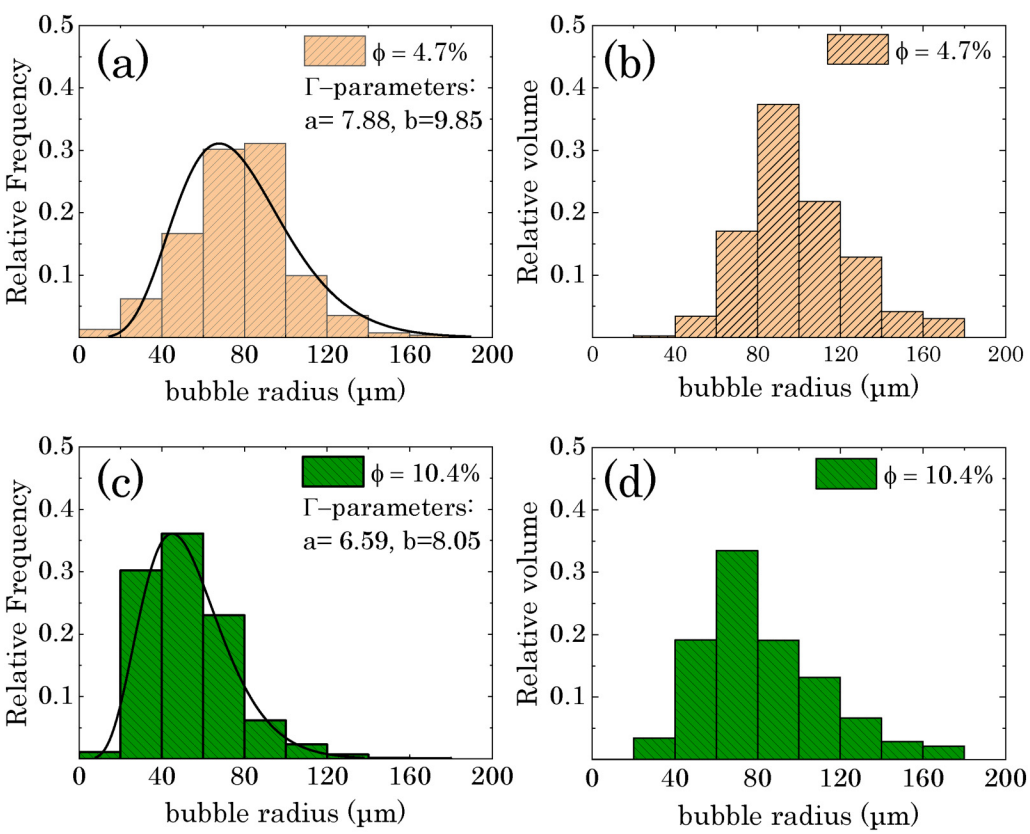

FIG. 7. Number-weighted bubble size distribution for (a) $\phi_1 = 4.7\%$ and (c) $\phi_2 = 10.4\%$; volume-weighted bubble size distribution for (b) $\phi_1 = 4.7\%$ and (d) $\phi_1 = 10.4\%$.

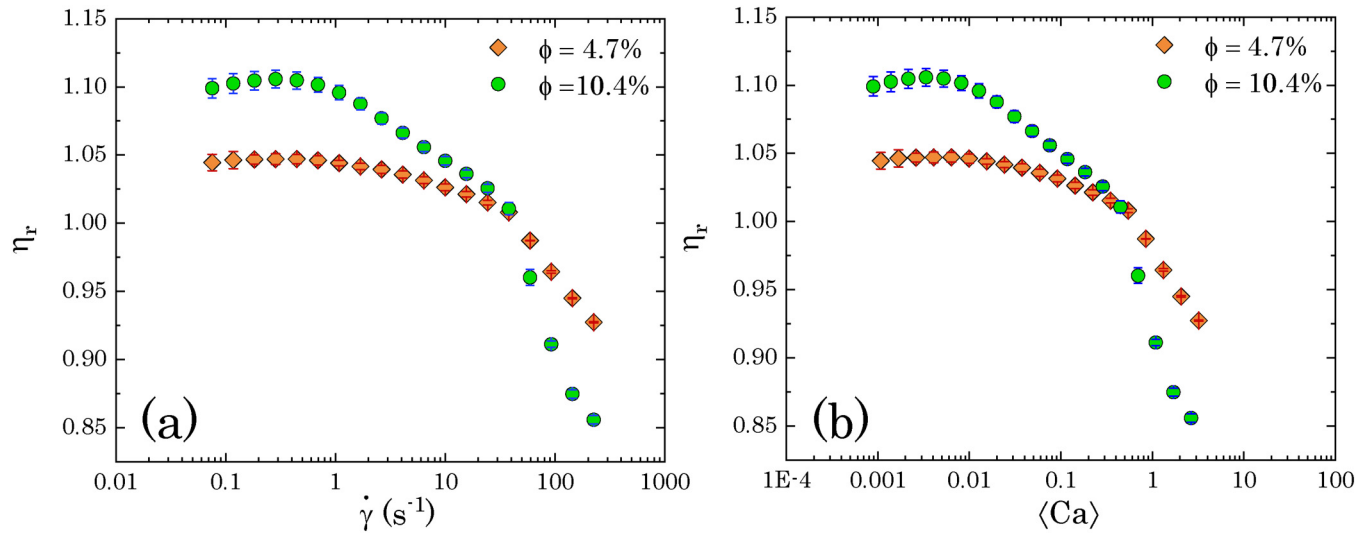

FIG. 8. (a) Relative viscosity as a function of shear rate for $\phi_1 = 4.7\%$ and $\phi_2 = 10.4\%$; (b) relative viscosity as a function of $\langle Ca \rangle$ for $\phi_1 = 4.7\%$ and $\phi_2 = 10.4\%$. Error bars represent the variation among three experimental repeats.

experiments, where the bubble sizes follow the gamma distribution. As shown in the theoretical examples, when the bubble sizes follow the gamma distribution, the suspension has a viscosity curve that is quite similar to that of a monodisperse suspension, the only difference being that the viscosity drop spans a larger range of $\langle Ca \rangle$ values. Having observed a different trend, we suspected that polydispersity could not be solely responsible for this behavior. To validate the above assumption, we compared our results with the theoretical polydisperse model of Mader *et al.* [7]. In Fig. 9, we present the experimental and theoretical relative viscosities as functions of $\langle Ca \rangle$ for the two reported polydisperse suspensions. As we see, there is good agreement between the real and theoretical values in the zero-shear plateau and in the second decay of viscosity. But, the polydisperse model does not predict the first decay of viscosity. Therefore, we can argue that the second decrease in viscosity is due to bubble deformation and polydispersity, but not the first decrease. To eliminate the possibility of elastic instabilities affecting the viscosity at higher shear rates, we checked our system with the criteria described by McKinley *et al.* [23,24] and Shaqfeh [25] for a plate-plate geometry. We observed that even for the highest tested shear rate, the suspensions do not fulfil the criteria for the onset of elastic instabilities, hence confirming that the second decay of viscosity is not due to this effect.

To ensure that the first decrease of viscosity is not related to a stress overshoot or any other time-dependent phenomena, we performed start-up shear experiments, shearing the suspensions for 40 s at $\dot{\gamma} = 0.5$, 5, and 50 s^{-1}. The recorded transient data confirmed that there were no unexpected features in the viscosity trends with time. We also performed shear tests, where the shear rate was consecutively ramped up and down to investigate the thixotropic character of the

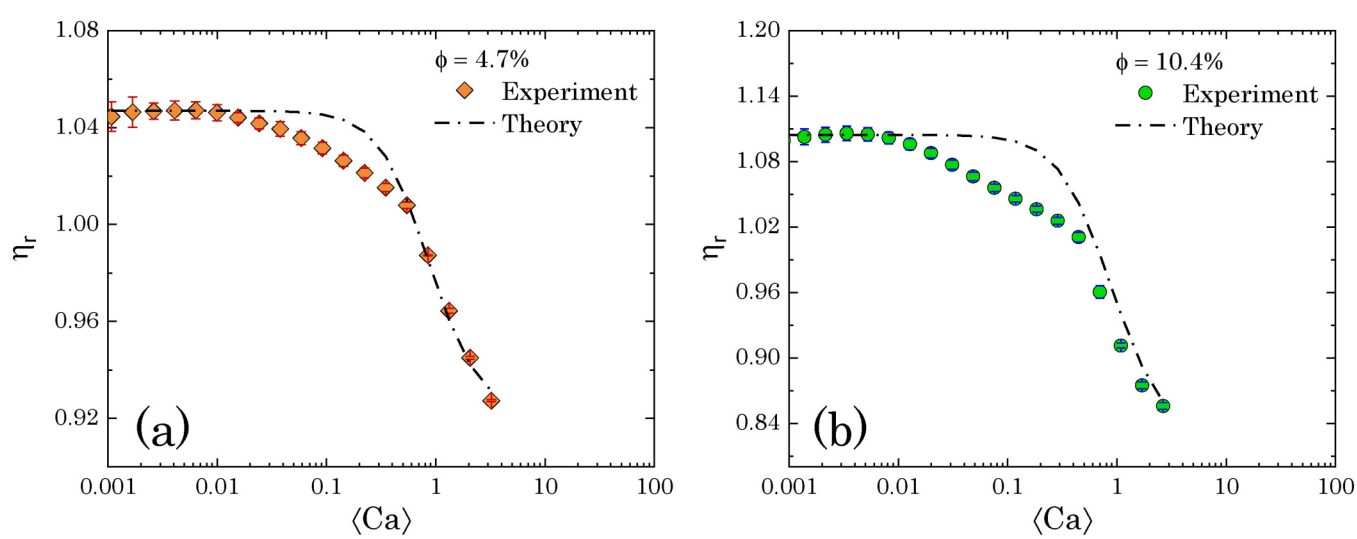

FIG. 9. Experimental versus theoretical relative viscosity for polydisperse bubble suspensions with (a) $\phi_1 = 4.7\%$ and (b) $\phi_2 = 10.4\%$. Error bars represent the variation among three experimental repeats.

dispersions. However, these tests could not give reliable information about our samples. This is because the bubble suspensions do not preserve the initial structure after being sheared at medium-/high-shear rates, where bubble deformation and coalescence become dominant. Thus, to investigate the cause of the first decay of viscosity, we visualized the dynamic behavior of the bubble suspensions under shear.

V. VISUALIZATION OF BUBBLES UNDER STEADY SHEAR FLOW

To visualize bubbles under shear, we prepared three fresh semidilute polydisperse bubble suspensions. The volume fractions of these new suspensions were $\phi_1 = 5.6\%$, $\phi_2 = 7.23\%$, and $\phi_3 = 8.52\%$. Figure 10 presents some representative images for the suspension with bubble volume fraction ϕ_2, taken with a 1.9 mm gap, at shear rates 0.1 and $23\,\mathrm{s}^{-1}$. At shear rates of order $0.1\,\mathrm{s}^{-1}$, the bubbles are uniformly dispersed. As the shear rate increases, bubbles start aligning to form bubble threads or getting closer to each other, forming clusters. We observed that the shear-induced bubble clustering was three-dimensional and dynamic, with threads and clusters breaking and reforming continuously throughout the entire samples. The phenomenon became progressively more evident in the shear rate range $1\,\mathrm{s}^{-1}$ to $23\,\mathrm{s}^{-1}$, where we also noticed the first decay of viscosity. Feneuil *et al.* [26] confirmed the formation of bubble clusters and threads under steady shear flow. According to them, the phenomenon is mainly due to bubble deformation and, thus, occurs only when the capillary number is large enough; that is, $Ca > 0.2$ for their experiments. However, this is not the case in our suspensions, where the formation of bubble clusters and threads started at average capillary numbers smaller than 0.2. At this point, it is worth clarifying that the model of Mader *et al.* [7] does not account for bubble clustering and alignment, so the deviation between the experimental and the theoretical values in the first decay of viscosity is reasonable. The model simply suggests the linear additivity of the contributions of the different bubble classes in a polydisperse system, whose viscosity is calculated with the constitutive equation developed by Llewellin *et al.* [6] for a monodisperse suspension [Eq. (6)]. As discussed, this constitutive equation was derived from the equation of Frankel and Acrivos [16], which recovers Taylor's equation [17] for $Ca \ll 1$ and does not contain second- or higher- orders terms of the dispersed-phase volume fraction so that it cannot account for complex phenomena arising from bubble interactions, such as bubble clustering and/or alignment.

Apart from bubble clustering, at higher $\langle Ca \rangle$, we also observed bubble coalescence and deformation. Finally, the optical measurements also confirmed the absence of any bubble rise in the duration of our experiments (whose total time was 11 min). The issue of bubble rise becomes important in long stationary experiments, where the bubbles experience only buoyancy. However, under steady shear, bubble rise is retarded due to flow in the tangential direction. Moreover, the use of surfactants, as in our experiments, can reduce the rising velocity of small bubbles by up to 50% [27,28]. For all these reasons, we believe that bubble rise was negligible and did not affect our experimental results.

A. Statistical analysis

1. Coverage

To quantify the shear-induced bubble clustering, we performed a statistical image analysis, defining the following dimensionless parameter, named *coverage*:

$$C \equiv \frac{\text{Total bubble surface (in pixels)}}{\text{Image surface (in pixels)}}. \tag{21}$$

C represents the percentage of the image covered with bubbles. When bubbles are close enough to form threads and clusters, we expect a greater overlapping of bubbles and a

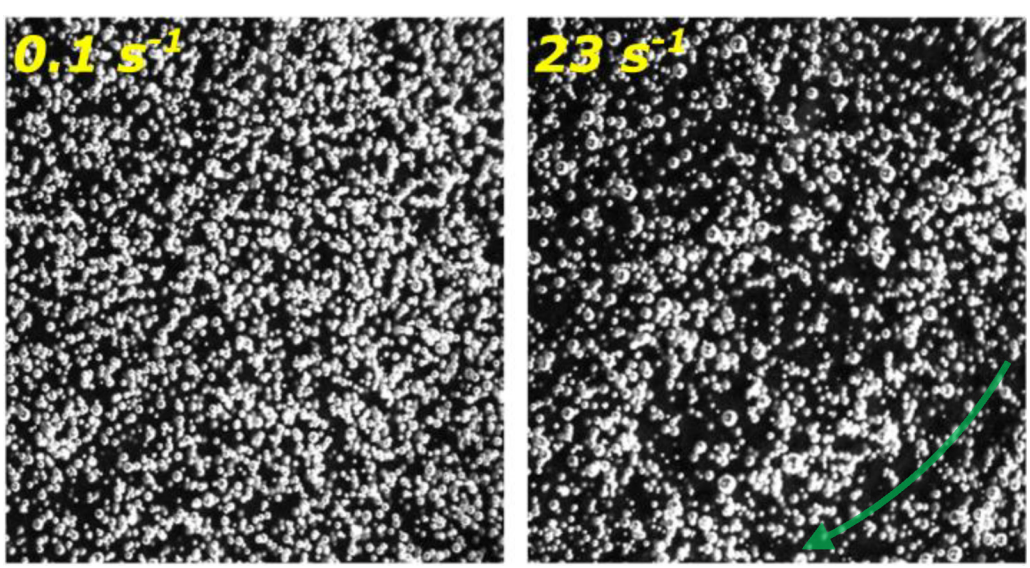

FIG. 10. Bubble suspension ($\phi = 7.23\%$) under steady shear at 0.1 and $23\,\mathrm{s}^{-1}$ (1.9 mm gap). The arrow indicates the direction of the flow.

decrease in the area of the image occupied by bubbles, with a resulting decrease in coverage. Thus, a reduction in coverage can be used as a measure for bubble clustering. This can be visually confirmed with the images presented in Fig. 10. As we see, for shear rate 23 s^{-1}, where bubble threads and clusters are present, the image seems less covered with bubbles compared to the case with shear rate 0.1 s^{-1}, where the bubbles are uniformly dispersed. To minimize the amount of data, we conducted the analysis using 30 representative images out of the 600 obtained for each shear rate. Since we were shearing for 40 s at each shear rate, we selected the images that corresponded to the time interval during which a steady state had been attained. This happened typically within the first 50 images. Each image was first converted into a black and white matrix, with the bubbles depicted as white pixels on a black background. Then, we summed all the white pixels and divided them by the total number of pixels in the image. For each shear rate, we calculated a mean coverage, $\overline{C}$, obtained by averaging over the coverage values of the 30 images. In Fig. 11, we present the average coverage as a function of the average capillary number for the tested suspensions. As seen, $\overline{C}$ always increased up to $\langle Ca \rangle \approx 0.005$ and then decreased continuously in the range of shear rates observed. The coverage parameter is a qualitative metric for bubble clustering, meaning that one should focus on the general trend and not on the absolute values. The decrease in $\overline{C}$ validates the optical observations, confirming the formation of bubble clusters and threads around $\langle Ca \rangle \sim 0.01$. We believe that the initial increase is due to bubble redistribution in the sample. Similar to particle suspensions during preshearing, bubbles disperse at low shear rates, removing any nonuniform bubble distribution formed during sample loading in the rheometer. Moreover, the coverage increased with the bubble volume fraction for all shear rates tested. This behavior is reasonable since larger bubble volume fractions lead to an increase in the total bubble surface and, thus, to larger values of coverage.

2. *Bubble coalescence*

To ensure that the initial bubble size distribution did not change significantly during the rheological tests, we investigated how the sizes of the bubbles changed with shear. To do so, we used the 0.8 mm gap images because they allowed identifying the bubbles more precisely. Using MATLAB, we identified the bubbles and their radii in pixels for each image. To convert pixels into mm, we attached a 1 mm calibration tape on the glass bottom plate. The scale was found to be equal to 306 pixels/mm. For each image, we determined the bubble size distribution, which was always of a gamma type, and calculated the De Brouckere average diameter d_{43}. For each shear rate, we evaluated the mean De Brouckere diameter by averaging the d_{43} values obtained for 30 different images. In Fig. 12, we indicatively present how $\langle d_{43} \rangle$ changed for the suspension with $\phi = 7.23\%$. As seen, the bubble size is increased by 16.4%. As mentioned earlier, this value might have been slightly enhanced compared to the 1.9 mm gap tests due to the smaller gap used for this analysis. Hence, even with the use of surfactants, there was some bubble coalescence, but this did not affect the average bubble size significantly.

B. Bubble clustering and shear-thinning

As shown by the statistical image analysis, bubbles started aligning/clustering at shear rates around 1 s^{-1} ($\langle Ca \rangle \sim 0.01$), where we also observed the first decay of viscosity. Therefore, we believe that the formation of bubble threads and clusters is responsible for the first shear-thinning trend. Specifically, when bubbles align, the total bubble area exposed to the flow decreases; thus, the distortion of the fluid streamlines due to the presence of the bubbles and, in turn, the suspension viscosity, reduces. Ordering in the direction of the fluid streamlines does not apply only to single bubbles but also to the 3D dynamic bubble clusters, observed during the rheo-optical experiments. Moreover, when bubbles are positioned very close to each other, forming

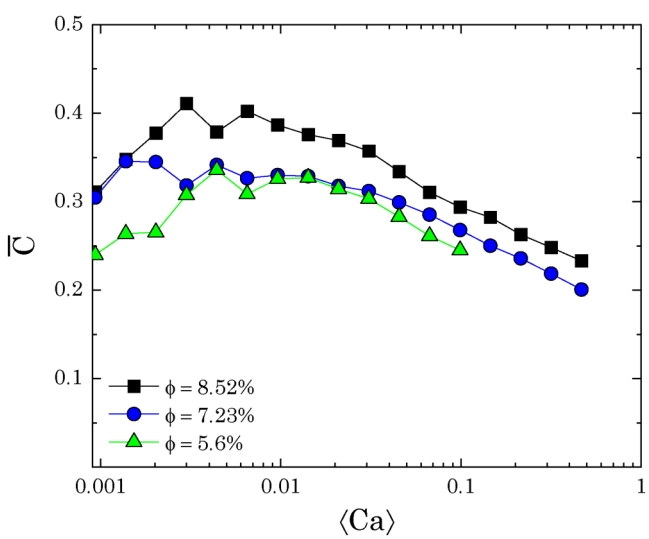

FIG. 11. Coverage as a function of $\langle Ca \rangle$ for $\phi_1 = 5.6\%$, $\phi_2 = 7.23\%$, and $\phi_3 = 8.52\%$.

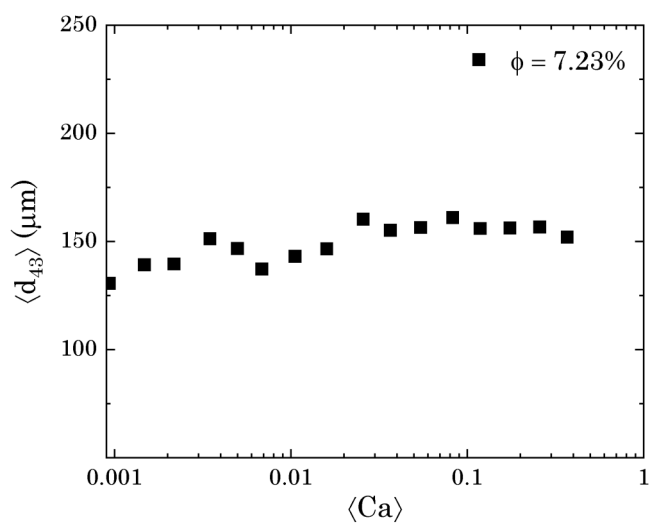

FIG. 12. Mean De Brouckere average diameter $\langle d_{43} \rangle$ as a function of $\langle Ca \rangle$ for $\phi = 7.23\%$.

clusters, there is no flow in the interstitial spaces. The fluid streamlines do not distort within the clusters, but only around them. Consequently, the flow resistance is smaller for bubble clusters compared with randomly positioned bubbles.

Microstructure changes and higher order phenomena, such as clustering and alignment, have been associated with shear-thinning behavior in multiple occasions. Recent works [29–31] showed that the formation of solid particle aggregates at lower shear rates and their later breakdown and alignment with the fluid streamlines at increasing shear rates lead to a decrease in suspension viscosity. Comparing bubble and particle suspensions, one can identify both similarities and differences in the mechanism of clustering-induced shear-thinning. The similarity lies in the core of the shear-thinning mechanism, which is common for both particle and bubble suspensions and regards the ordering of either individual particles/bubbles or particle/bubble clusters in the direction of the fluid streamlines. However, the way this ordering happens is different for each case. For particle suspensions, the shear-thinning behavior is observed when the aggregates break down, while for bubble suspensions in the semidilute regime, we observed that the shear-thinning onset coincided with the formation of bubble clusters and threads. This contrast can be explained by considering the different nature of the two systems. Particle aggregates are usually formed in concentrated systems due to attractive forces between the particles. This results in a highly structured network of clusters with restrained movement and rotation, which, at lower shear rates, opposes the flow and results in higher suspension viscosity. As the shear rate increases, the particle aggregates break down and start aligning with the fluid streamlines, causing the shear-thinning behavior. However, for semidilute bubble suspensions, the nature of the shear-induced clusters is different. Since the bubble suspensions are not concentrated, the generated dynamic bubble clusters are free to move and align in the direction of the fluid streamlines, causing the first shear-thinning trend we observed in our rheological experiments.

VI. CONCLUSIONS

In this work, we described the complex shear-thinning behavior of semidilute polydisperse bubble suspensions under steady shear, by explaining the effect of polydispersity and shear-induced clustering. To do so, we generated semidilute polydisperse bubble suspensions with a mixture of mineral oil and 0.57 mol/l Span80 (surfactant) as ambient fluid, and then measured their steady shear viscosity. The bubble sizes of the produced polydisperse suspensions were found to follow a distribution between 10 and 170 μm. We confirmed that polydispersity can cause an extended shear-thinning behavior, which spans a larger range of average capillary number values, instead of happening at $\langle Ca \rangle \sim 1$. However, the effect of polydispersity becomes important only if the total bubble volume fraction is evenly divided between very small and very large bubbles. Under real experimental conditions, where the bubble sizes follow the gamma distribution, we can regard the polydisperse suspension as monodisperse with a diameter equal to the volume-weighted average diameter.

However, the flow curves obtained from our experimental investigations showed an unexpected double power-law decay in the suspension viscosity, the first decrease happening at $\langle Ca \rangle \sim 0.01$ and the second at $\langle Ca \rangle \sim 1$. Comparing our experimental results with the polydisperse viscosity model of Mader *et al.* [7], we found good agreement in the zero-shear viscosity plateau and the second decay of viscosity, but the model failed to predict the first viscosity drop. Thus, we believe that unlike the second shear-thinning trend, the first is unrelated to bubble deformation and polydispersity.

To investigate further the first decrease of viscosity, we visualized the bubble suspensions under steady shear. We performed a statistical image analysis, which showed that bubbles started aligning/clustering at $\langle Ca \rangle \sim 0.01$. The image analysis also revealed that at higher shear rates, bubbles deform and coalesce, with the average bubble diameter increasing by 16.4%, an increase that, however, cannot explain the first decay of viscosity observed. Therefore, we believe that the first decrease in viscosity is due to the formation of bubble threads and clusters and their ordering across the direction of the flow, which, in turn, causes less distortion of the fluid streamlines and, hence, a decrease in suspension viscosity.

ACKNOWLEDGMENTS

The authors wish to thank Simon Dawes from the Chemical Engineering Workshop at UCL for help in setting up the experimental apparatus and acknowledge GlaxoSmithKline Consumer Healthcare and the EPSRC (Formulation Grant CORAL, No. EP/N024915/1) for the financial support given to this project.

AUTHOR DECLARATIONS

Conflict of Interest

The authors have no conflicts to disclose.

DATA AVAILABILITY

The data that support the findings of this study are available from the corresponding authors upon reasonable request.

REFERENCES

[1] Manga, M., and M. Loewenberg, "Viscosity of magmas containing highly deformable bubbles," J. Volcanol. Geotherm. Res. **105**, 19–24 (2001).

[2] Campbell, G. M., and E. Mougeot, "Creation and characterisation of aerated food products," Trends Food Sci. Technol. **10**, 283–296 (1999).

[3] Ahmed, R. M., N. E. Takach, U. M. Khan, S. Taoutaou, S. James, A. Saasen, and R. Godøy, "Rheology of foamed cement," Cem. Concr. Res. **39**, 353–361 (2009).

[4] Malysa, K., and K. Lunkenheimer, "Foams under dynamic conditions," Curr. Opin. Colloid Interface Sci. **13**, 150–162 (2008).

[5] Llewellin, E. W., H. M. Mader, and S. D. R. Wilson, "The rheology of a bubbly liquid," Proc. R. Soc. A **458**, 987–1016 (2002).

[6] Llewellin, E. W., H. M. Mader, and S. D. R. Wilson, "The constitutive equation and flow dynamics of bubbly magmas," Geophys. Res. Lett. **29**, 23-1–23-4, https://doi.org/10.1029/2002GL015697 (2002).

[7] Mader, H., E. Llewellin, and S. Mueller, "The rheology of two-phase magmas: A review and analysis," J. Volcanol. Geotherm. Res. **257**, 135–158 (2013).

[8] Rust, A., and M. Manga, "Effects of bubble deformation on the viscosity of dilute suspensions," J. Non-Newtonian Fluid Mech. **104**, 53–63 (2002).

[9] Sibree, J. O., "The viscosity of froth," Trans. Faraday Soc. **30**, 325–331 (1934).

[10] Stein, D. J., and F. J. Spera, "Rheology and microstructure of magmatic emulsions: Theory and experiments," J. Volcanol. Geotherm. Res. **49**, 157–174 (1992).

[11] Sura, V. M., and P. C. Panda, "Viscosity of porous glasses," J. Am. Ceram. Soc. **73**, 2697–2701 (1990).

[12] Bagdassarov, N., and D. Dingwell, "A rheological investigation of vesicular rhyolite," J. Volcanol. Geotherm. Res. **50**, 307–322 (1992).

[13] Bagdassarov, N. S., and D. B. Dingwell, "Frequency dependent rheology of vesicular rhyolite," J. Geophys. Res.: Solid Earth **98**, 6477–6487, https://doi.org/doi:10.1029/92JB02690 (2002 (1993).

[14] Lejeune, A., Y. Bottinga, T. Trull, and P. Richet, "Rheology of bubble-bearing magmas," Earth Planet. Sci. Lett. **166**, 71–84 (1999).

[15] Stein, D. J., and F. J. Spera, "Shear viscosity of rhyolite-vapor emulsions at magmatic temperatures by concentric cylinder rheometry," J. Volcanol. Geotherm. Res. **113**, 243–258 (2002).

[16] Frankel, N. A., and A. Acrivos, "The constitutive equation for a dilute emulsion," J. Fluid Mech. **44**, 65–78 (1970).

[17] Taylor, G. I., "The viscosity of a fluid containing small drops of another fluid," Proc. R. Soc. A **138**, 41–48 (1932).

[18] Einstein, A., Eine neue bestimmung der moleküldimensionen, Ph.D. dissertation, ETH Zurich, 1905.

[19] Mendoza, C. I., and I. Santamaría-Holek, "The rheology of hard sphere suspensions at arbitrary volume fractions: An improved differential viscosity model," J. Chem. Phys. **130**, 044904 (2009).

[20] Cross, M. M., "Rheology of non-newtonian fluids: A new flow equation for pseudoplastic systems," J. Colloid Sci. **20**, 417–437 (1965).

[21] Morini, R., X. Chateau, G. Ovarlez, O. Pitois, and L. Tocquer, "Steady shear viscosity of semi-dilute bubbly suspensions," J. Non-Newtonian Fluid Mech. **264**, 19–24 (2019).

[22] Macosko, C. W., *Rheology: Principles, Measurements and Applications* (Wiley-VCH, Inc., New York, 1994).

[23] McKinley, G. H., J. A. Byars, R. A. Brown, and R. C. Armstrong, "Observations on the elastic instability in cone-and-plate and parallel-plate flows of a polyisobutylene Boger fluid," J. Non-Newtonian Fluid Mech. **40**, 201–229 (1991).

[24] McKinley, G. H., P. Pakdel, and A. Öztekin, "Rheological and geometric scaling of purely elastic flow instabilities," J. Non-Newtonian Fluid Mech. **67**, 19–47 (1996).

[25] Shaqfeh, E. S. G., "Purely elastic instabilities in viscometric flows," Annu. Rev. Fluid Mech. **28**, 129–185 (1996).

[26] Feneuil, B., K. T. Iqbal, A. Jensen, L. Brandt, O. Tammisola, and A. Carlson, "Experimental and numerical investigation of bubble migration in shear flow: Deformability-driven chaining and repulsion," 10.48550/arXiv.2205.06575 (2022).

[27] De Kee, D., R. P. Chhabra, and A. Dajan, "Motion and coalescence of gas bubbles in non-newtonian polymer solutions," J. Non-Newtonian Fluid Mech. **37**, 1–18 (1990).

[28] Tzounakos, A., D. G. Karamanev, A. Margaritis, and M. A. Bergougnou, "Effect of the surfactant concentration on the rise of gas bubbles in power-law non-newtonian liquids," Ind. Eng. Chem. Res. **43**, 5790–5795 (2004).

[29] Papadopoulou, A., J. J. Gillissen, H. J. Wilson, M. K. Tiwari, and S. Balabani, "On the shear thinning of non-Brownian suspensions: Friction or adhesion?," J. Non-Newtonian Fluid Mech. **281**, 104298 (2020).

[30] Yang, Y., A. Oztekin, S. Neti, and S. Mohapatra, "Particle agglomeration and properties of nanofluids," J. Nanopart. Res. **14**, 852–862 (2012).

[31] Yokozeki, T., S. Schulz, S. Buschhorn, and K. Schulte, "Investigation of shear thinning behavior and microstructures of MWCNT/epoxy and CNF/epoxy suspensions under steady shear conditions," Eur. Polym. J. **48**, 1042–1049 (2012).